Laminar turbulent behavior in shear-thickening channel flow

Emanuele Milocco [1,2], Georgios Giamagas [3], Francesco Zonta [4], and Alfredo Soldati [1,2]
[1]*Institute of Fluid Mechanics and Heat Transfer, TU-Wien, 1060 Vienna, Austria*
[2]*Polytechnic Department, University of Udine, 33100 Udine, Italy*
[3]*University of Grenoble Alpes, LEGI, G-INP, CNRS, 38000 Grenoble, France*
[4]*School of Engineering, Newcastle University, Newcastle upon Tyne NE1 7RU, United Kingdom*

(Received 23 December 2024; accepted 6 June 2025; published 7 July 2025)

We conduct direct numerical simulations (DNS) to investigate the dynamics of a non-Newtonian shear-thickening fluid in a turbulent plane channel. The primary parameter governing the non-Newtonian flow rheology is the Carreau number (Cu), defined as the ratio of the fluid's characteristic timescale, Λ, to the flow characteristic timescale, h/u_τ, where h is the channel half-height and u_τ is the friction velocity at the wall. Starting from a Newtonian turbulent channel flow at $\mathrm{Re}_\tau = 180$, we examine the impact of increasing Cu on turbulent statistics and coherent structures. The shear-dependent rheology is described using a Carreau viscosity model, with Cu values spanning two orders of magnitude ($\mathrm{Cu} = 0.1, 1, 5, 10$). While maintaining a constant mean pressure gradient ($\nabla\overline{p}$) that drives the flow—ensuring a fixed shear Reynolds number based on the zero-strain-rate reference viscosity $\mathrm{Re}_{\tau,0} = 180$—we observe varying effective Reynolds numbers ($\mathrm{Re}_{\tau,w} = 111, 76, 58, 52$) due to the altered viscosity distributions. Our findings reveal that shear thickening generally reduces the mean flow velocity and enhances the isotropy of velocity fluctuations compared to the Newtonian reference case. As Cu increases, the strength of vortical structures diminishes, accompanied by a decline in turbulence intensity. This behavior is primarily attributed to elevated wall viscosity, which shifts turbulent stresses towards viscous stresses. Notably, at subcritical effective shear Reynolds numbers for which a Newtonian fluid would exhibit laminar flow, the shear-thickening fluid retains unsteady behavior (turbulence) but lacks a logarithmic layer.

DOI: 10.1103/xn5s-7jsc

I. INTRODUCTION

Understanding the dynamics of turbulent flows involving non-Newtonian fluids in pipes and ducts is critically important for numerous industrial and environmental applications [1,2]. Notable examples include the transport of polymeric solutions and slurries in the chemical, biomedical, and process industries, the lubrication of biological fluids [3–5], and the flow of food products in the food and beverage industry [2,6,7]. In contrast to Newtonian fluids, non-Newtonian fluids exhibit complex viscosity behavior, which varies with shear rate. This characteristic makes predicting the flow patterns of non-Newtonian fluids particularly challenging, especially under turbulent flow conditions. In the literature, non-Newtonian rheological behavior is often modeled by representing the fluid as a mixture of a solid-phase suspension with small characteristic size dispersed in a Newtonian carrier phase [8–10]. The non-Newtonian properties arise from the

small particles—of characteristic length scale a—suspended within the liquid phase. The particle Reynolds number, $\mathrm{Re}_p = \rho\dot{\gamma}a^2/\mu_{eq}$, defined using an equivalent dynamic viscosity μ_{eq} and a strain rate $\dot{\gamma} = (2\mathbf{SS})^{1/2}$—where $\mathbf{S}$ is the shear rate tensor—is generally very low, allowing the particles to be considered inertialess.

The viscoelastic and time-dependent nature of these fluids, characterized by partial elastic recovery and additional dissipation, is strongly influenced by the solid fraction. In most engineering applications, viscoelastic effects are negligible [10], allowing the fluid to be modeled as a generalized-Newtonian fluid (GNF). Note that GNFs are a class of purely viscous, time-independent fluids that adhere to the following constitutive relation:

$$\tau = \mu_a(\dot{\gamma})\mathbf{S} = \mu_a(\dot{\gamma})[\boldsymbol{\nabla}\mathbf{u} + (\boldsymbol{\nabla}\mathbf{u})^{\mathbf{T}}], \tag{1}$$

where τ is the shear stress and $\mu_a(\dot{\gamma})$ represents the apparent viscosity.

Non-Newtonian fluids can be broadly categorized into two types: shear-thickening fluids, where the apparent viscosity increases with strain rate, and shear-thinning fluids, where the apparent viscosity decreases as the strain rate rises. This study focuses exclusively on the flow of shear-thickening fluids inside a channel.

Shear thickening was first observed almost a century ago by Freundlich and Röder [11] for dense suspensions, and later received increasing attention because of its seemingly important role in the blockage of small ducts/pipelines in crude oil transportation [12]. Reportedly, the flow of shear-thickening fluids is characterized by a larger drag compared to the flow of a Newtonian fluid [13,14]. The adoption of shear-thickening fluids is thus constrained to specific applications, where the ability of dissipating/absorbing energy is required: these include vibration absorption [15], body armors [16], or, more in general, when the transportation of a solid dispersed phase by a carrier fluid is needed [12]. Among the most important examples of shear-thickening fluids in the process/food industry are oobleck, chocolate (before the addition of lecithin and the conching process [17]), and a titanium dioxide TiO_2-water suspension. The latter is the most widely used natural and nontoxic white pigment. In paints, food colourant and coatings, $TiO_2$is adopted for its bright characteristics (it is often referred to as white titanium). Moreover, the low diameter (order of a few μm) distribution of particles inside this fluid system opens the possibility of scattering low-frequency light and UV much more easily (quantified by the hiding power, HP, which is the ability to hide the surface of an object). The higher the volume fraction of the dispersed solid phase is, the more the reflective properties of the white paint are, thus enabling indirect energy savings. One of the first experimental rheological investigations of this solution and on the role of the white pigment concentration was carried out by Metzner and Whitlock [18], who showed that for low volume fractions ($\phi < 0.47$), the TiO_2-water system acts as a continuous shear-thickening fluid (CST), characterized by a gradual increase in viscosity with the strain rate. However, if the limit is surpassed the system behaves discontinuously, with markedly different rheological behavior. The discontinuous shear-thickening fluid (DST) suspension is characterized by a sudden increase in $\mu_a(\dot{\gamma})$ over a narrow range of strain rate $\dot{\gamma}$: $\partial\mu_a/\partial\dot{\gamma} \to \infty$ [9]. Clearly a fluid of this type should be avoided in industrial applications because any off-regime operation might cause severe and irreversible damage to equipment such as pumps, pipes, mixers, and other devices [19].

Unlike shear-thinning fluids, which have been extensively studied in the literature ([13,20–22]), shear-thickening fluids have received comparatively less attention. This is primarily due to the challenges associated with obtaining accurate experimental measurements, as these experiments typically rely on optical techniques that are difficult to apply to inherently non-transparent fluids, such as shear-thickening fluids [23]. Only recently have theoretical and computational approaches become more popular, providing precise space- and time-resolved data for entire flow fields across various flow configurations and fluid properties or microstructures [13,14,24–26].

In this work we use direct numerical simulations (DNSs) to study the dynamics of a turbulent channel flow of a continuous shear-thickening fluid, the rheology of which is described via a

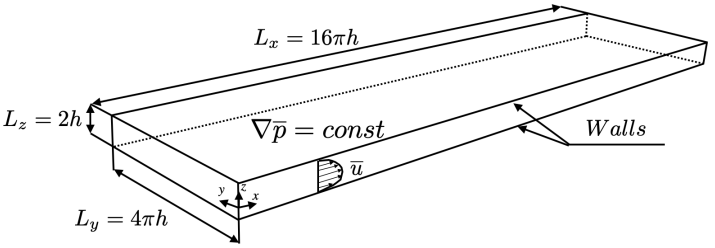

FIG. 1. Sketch of the computational setup used for the simulations. The channel has dimensions $L_x \times L_y \times L_z = 16\pi h \times 4\pi h \times 2h$. A constant pressure gradient $\nabla\overline{p}$ is imposed into the system to drive the flow, which goes from left to right.

Carreau model [27,28]. Keeping the fluid properties and the imposed pressure gradient (to drive the flow) constant, we study the effect of varying the Carreau number, Cu, over a broad range of values $0.1 < \mathrm{Cu} < 10$. In particular, we try to elucidate the role of the viscosity distribution on the overall flow structure. We remark here that, among the different rheology models available for GN fluids—chiefly the power-law (PL) and the Cross ones, which are based on the interpolation of experimental measurements obtained from a rheogram—the Carreau model has the advantage of being a physically sound model, derived from the molecular network theories [27,28]. It has also better performances in capturing the apparent viscosity at low and large strain rate values.

The paper is organized as follows: in Sec. II we present the numerical methodology and the setup employed to perform the simulations, while in Sec. III we present and discuss the results of the simulations in terms of first- and second-order turbulent statistics and shear stress budget. Finally, in Sec. IV we draw our conclusions.

II. METHODOLOGY

A. Direct numerical simulations

We consider a continuous shear-thickening single phase flow moving inside a horizontal channel geometry under the action of an imposed pressure gradient. The channel dimensions are $L_x \times L_y \times L_z = 16\pi h \times 4\pi h \times 2h$, where h is the half channel height while the streamwise, spanwise, and the wall normal coordinates are denoted by x, y, z, respectively. A schematic visualization of the computational domain is highlighted in Fig. 1. The fully resolved flow is described by the continuity and momentum equations, which accounts for a nonuniform viscosity $\mu_a(\dot{\gamma})$ due to the shear-thickening rheology:

$$\boldsymbol{\nabla}\cdot\mathbf{u} = 0, \quad \rho\frac{\partial\mathbf{u}}{\partial t} + \rho\mathbf{u}\cdot\boldsymbol{\nabla}\mathbf{u} = -\boldsymbol{\nabla}p + \boldsymbol{\nabla}\cdot\{\mu_a(\dot{\gamma})[\boldsymbol{\nabla}\mathbf{u} + (\boldsymbol{\nabla}\mathbf{u})^{\mathbf{T}}]\}, \tag{2}$$

where $\mathbf{u} = (u, v, w)$ is the velocity vector, p is the pressure, ρ is the fluid density, and $\dot{\gamma} = \sqrt{2\mathbf{S}:\mathbf{S}}$ is the strain rate, with the shear rate tensor defined as $\mathbf{S} = 1/2(\boldsymbol{\nabla}\mathbf{u} + \boldsymbol{\nabla}\mathbf{u}^{\mathsf{T}})$.

The approach adopted here to handle the diffusive term follows the methodology used in [29]. Specifically, the viscosity $\mu_a(\dot{\gamma})$ is decomposed into a spatially constant component, μ_{ref}, and a variable component, $\mu_a(\dot{\gamma}) - \mu_{\mathrm{ref}}$, which is a function of the strain rate and, thus, the position inside the channel. Consequently, the total viscous term can be expressed as

$$\boldsymbol{\nabla}\cdot\{\mu_a(\dot{\gamma})[\boldsymbol{\nabla}\mathbf{u} + (\boldsymbol{\nabla}\mathbf{u})^{\mathbf{T}}]\} = \mu_{\mathrm{ref}}\nabla^2\mathbf{u} + \boldsymbol{\nabla}\cdot\{[\mu_a(\dot{\gamma}) - \mu_{\mathrm{ref}}](\boldsymbol{\nabla}\mathbf{u} + \boldsymbol{\nabla}\mathbf{u}^{\mathbf{T}})\}. \tag{3}$$

The governing equations are discretized using a pseudospectral method, transforming the field variables into the wavenumber space. Fourier representations are used for the periodic

(homogeneous) directions x and y, while a Chebyshev representation is employed for the wall-normal (nonhomogeneous) direction z. Periodic boundary conditions are assumed in the x and y directions for the velocity field $\mathbf{u}$, and no-slip conditions, $\mathbf{u} = 0$, are assumed at the two walls located at $z = \pm h$. The time integration of the uniform term in Eq. (3), $\mu_{\text{ref}}\nabla^2\mathbf{u}$, is handled implicitly using a Crank-Nicolson scheme. The remaining term, which depends on the velocity field, is treated explicitly and integrated using an Adams-Bashforth scheme together with the other nonlinear terms of Eq. (2). Further details can be found in [29].

B. Viscosity of the shear-thickening fluid

We treat the shear-thickening fluid as continuous and homogeneous, modeling it as an isothermal generalized-Newtonian (GN) fluid with apparent viscosity $\mu_a(\dot{\gamma})$, which depends on the strain rate $\dot{\gamma}$, is independent of time and can be described adopting the constitutive Carreau equation:

$$\mu_a = \mu_\infty + (\mu_0 - \mu_\infty)[1 + (\Lambda\dot{\gamma})^2]^{(n-1)/2} \tag{4}$$

where μ_∞ and μ_0 are, respectively, the ideal viscosities at infinite and zero strain rates (which are usually known *a priori* because they do not depend on the flow field), Λ is the fluid characteristic timescale and n is the flow index, which characterize the non-Newtonian rheology. For $n = 1$, the Carreau model reduces to a Newtonian fluid with constant viscosity; for $0 < n < 1$, the fluid exhibits shear-thinning behavior, while for $n > 1$, it exhibits shear-thickening behavior.

In the following problem length and velocity scales are made dimensionless using the half-channel height h and the shear velocity $u_\tau = \sqrt{\tau_w/\rho}$, where τ_w represents the wall shear stress, as reference quantities. The apparent non-Newtonian viscosity is made dimensionless using the reference viscosity $\mu_{\text{ref}} = \mu_0$. Therefore the dimensionless strain rate reduces to $\tilde{\dot{\gamma}} = u_\tau/h\dot{\gamma}$, while the dimensionless viscosity, $\tilde{\beta} = \mu_a(x, y, z)/\mu_0$, representing the ratio of the apparent viscosity μ_a to the reference viscosity μ_{ref} becomes

$$\tilde{\beta} = \mu_\infty/\mu_0 + (1 - \mu_\infty/\mu_0)[1 + (\text{Cu}\text{Re}_{\tau,0}\tilde{\dot{\gamma}}^+)^2]^{(n-1)/2}. \tag{5}$$

Note that the symbol $\tilde{}$ indicates a dimensionless quantities. The Carreau number Cu is the ratio of the non-Newtonian timescale Λ to the characteristic channel flow timescale h/u_τ, $\text{Cu} = \Lambda u_\tau/h$ [30,31]. In the Carreau model, all fluid properties are known *a priori* by choosing the zero strain rate as the reference condition. The dimensionless quantity in Eq. (5) is the shear Reynolds number, $\text{Re}_{\tau,0} = \rho u_\tau h/\mu_0$, representing the ratio of inertial to viscous forces, and defined based on a reference viscosity at zero strain rate. Furthermore, this choice enables the strain rate to be expressed in wall units as $\tilde{\dot{\gamma}}^+ = 1/\text{Re}_{\tau,0}\tilde{\dot{\gamma}}$, i.e., using u_τ and μ_0 as reference quantities, and indicated by the superscript $^+$. In the following, unless otherwise noted, all quantities will be expressed in dimensionless form. However, the symbol $\tilde{}$ will be removed for ease of notation. Thus, the governing continuity and momentum Eq. (2), can be written in dimensionless form as

$$\nabla\cdot\mathbf{u} = 0, \quad \frac{\partial\mathbf{u}}{\partial t} + \mathbf{u}\cdot\nabla\mathbf{u} = -\nabla p + \nabla\cdot\left[\frac{\beta(\dot{\gamma}) - 1}{\text{Re}_{\tau,0}}(\nabla\mathbf{u} + \nabla\mathbf{u}^{\mathbf{T}})\right] + \frac{1}{\text{Re}_{\tau,0}}\nabla^2\mathbf{u}. \tag{6}$$

As previously stated, the rheological properties of the flow are defined by the Carreau number, Cu. The influence of the Carreau number Cu on the rheology map is illustrated in Fig. 2, by plotting the dimensionless viscosity β as a function of the strain rate $\dot{\gamma}$. We note that Cu influences the viscosity across the entire range of strain rates but has less influence in the region near the zero-strain-rate plateau, where the apparent viscosity μ_0 remains uniform and constant regardless of the value of Cu. The Carreau model also introduces the characteristic time $\Lambda = 1/\dot{\gamma}_t$, where $\dot{\gamma}_t$ is the strain rate (transition strain rate) at which the viscosity starts to deviate appreciably from its zero-strain-rate value [10,31]. This concept is illustrated in the inset of Fig. 2. For $\text{Cu} \to 0$, the viscosity is

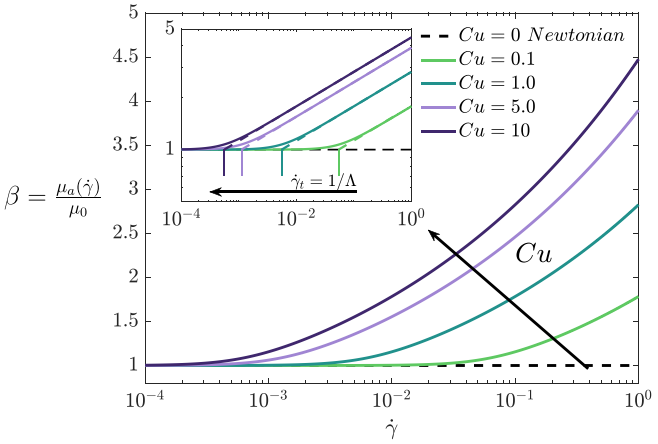

FIG. 2. Rheology map for the adopted shear-thickening cases. The nondimensional viscosity $\beta = \mu_a(\dot{\gamma})/\mu_0$ is plotted against the strain rate $\dot{\gamma}$ for different Carreau numbers Cu (see Table I). The inset illustrates the influence of the nondimensional fluid timescale Λ on the transition strain rate $\dot{\gamma}_t$, with the y axis (β) displayed in logarithmic scale. Increasing Λ reduces $\dot{\gamma}_t$, shifting the onset of shear thickening to lower strain rates. Note that the strain rate has been made dimensionless with $\mathrm{Re}_{\tau,0} = 180$, i.e., in wall units, and the flow index has been set to $n = 1.2$ to describe a continuous increase in viscosity.

approximately uniform and equal to the zero-strain-rate viscosity, $\beta = 1$. This indicates that the fluid behaves as Newtonian, with a constant and uniform viscosity μ_0 [31]. For $0.1 < \mathrm{Cu} < 10$, the rheology map behaves as shown in Fig. 2. As Cu increases, the range of fluid viscosity values broadens and the transition strain rate reached more rapidly, indicating stronger non-Newtonian behavior. For much larger Carreau number, $\mathrm{Cu} \gg 1$, viscosity increases sharply with $\dot{\gamma}$; however, in this case, the Carreau model is brought to the limit of its range of applicability.

Although originally formulated for shear-thinning fluids [27], the Carreau model can be extended to continuous shear-thickening behavior for $n > 1$. It is important to note that, at very high strain rates, the Carreau model predicts a divergence in viscosity—positive if $0 < \mu_\infty/\mu_0 < 1$ and negative if $\mu_\infty/\mu_0 > 1$—rather than asymptotically approaching μ_∞. This divergence is not relevant for the present study, as it occurs well beyond the strain-rate range considered here (see Fig. 2). Moreover, by adopting $\mu_\infty/\mu_0 < 1$, the Carreau model ensures a continuous, monotonic increase in viscosity with strain rate within the simulated range. This approach facilitates a smooth and numerically stable representation of continuous shear-thickening behavior, in accordance with previous studies [13]. From a physical viewpoint, and in the context of the dispersed solid-phase dense suspension, an increase in Cu can be achieved by increasing the volume fraction of the dispersed solid phase (i.e., increase of friction, and hence of the apparent viscosity, due to the larger surface area; see also experimental studies [32–34]).

C. Simulation set-up

We conducted one benchmark Newtonian simulation and four simulations for non-Newtonian Carreau fluid (CST) with constant fluid properties, and varying the Carreau number, from $\mathrm{Cu} = 0.1$ to $\mathrm{Cu} = 10$. In all simulations, the flow is driven by an imposed constant mean pressure gradient $\nabla\overline{p}$. In physical units the overall shear stress at the wall, τ_w, can be obtained from the force balance in the flow direction as

$$2\tau_w L_x L_y = \Delta\overline{p} L_y L_z, \tag{7}$$

TABLE I. Parameters used for the DNS at imposed pressure gradient $\nabla\overline{p}$ and theoretical flow condition at the centerline $\mathrm{Re}_{\tau,\mathrm{ref}} = \rho u_\tau h/\mu_0 = 180$. The bulk Reynolds number based on the reference viscosity $\mathrm{Re}_{b,0} = \rho\overline{u}h/\mu_0$ and the bulk viscosity ratio $\overline{\mu}/\mu_0$ are also included in the table.

Fluid	Cu	μ_0/μ_w	$\mathrm{Re}_{\tau,w}$	Δx^+	Δy^+	$\Delta z^+_{\max}$	$\mathrm{Re}_{b,0}$	$\overline{\mu}/\mu_0$
Newtonian (N1)	0	1.00	180	8.11	4.06	4.45	2860	1.00
Shear thickening (ST1)	0.1	0.62	111	5.49	4.43	2.45	2559	1.29
Shear thickening (ST2)	1.0	0.42	76	3.72	1.86	1.03	2441	2.36
Shear thickening (ST3)	5.0	0.32	58	2.85	1.43	0.79	2391	3.08
Shear thickening (ST3)	10.0	0.28	52	2.54	1.27	0.71	3244	3.48

where $\Delta\overline{p} = \overline{p}_{\mathrm{in}} - \overline{p}_{\mathrm{out}}$ is the pressure drop across the channel. The wall shear stress is thus given by

$$\tau_w = \frac{\Delta\overline{p}h}{L_x} = -\nabla\overline{p}h = \overline{\beta}_w \frac{\partial\overline{u}}{\partial z}\bigg|_w + \overline{\beta'_w \frac{\partial u'}{\partial z}}\bigg|_w. \tag{8}$$

Here the overbar, $\overline{()}$, denotes an ensemble-averaged quantity, while the prime symbol, $()'$, represents a fluctuating quantity (deviation from the average). Note that the fluctuating component of the stress does not vanish at the wall due to the influence of the turbulent flow field. By maintaining the same pressure gradient across all simulations, we ensure that the total wall shear stress remains consistent across cases. The viscous stress contribution arises from both Newtonian and non-Newtonian effects, which cannot be easily separated because the wall viscosity is *a priori* unknown. This occurs because, for a non-Newtonian fluid, the wall viscosity is a dynamic quantity that depends on the velocity field through the strain rate, $\dot{\gamma}$. Consequently, this evaluation is only possible *a posteriori*, based on the turbulent flow field. The wall viscosity, and thus the relative contributions of Newtonian and non-Newtonian stresses, will be determined as an outcome of the simulation. To ensure consistency across cases, we set a reference Reynolds number, $\mathrm{Re}_{\tau,0} = \rho u_\tau h/\mu_0 = 180$, based on the zero-strain-rate viscosity, μ_0. The range of viscosity values is defined by the ratio $\mu_\infty/\mu_0 = 10^{-4}$. The flow index is $n = 1.2$. This setup allows us to investigate the shear-thickening behavior of the fluid ($n > 1$), where viscosity increases with the strain rate. Note that the reference Reynolds number, $\mathrm{Re}_{\tau,0}$, is approximately equal to the local Reynolds number at the channel centerline, $\mathrm{Re}_{\tau,z=0}$, where the mean shear stress is zero. However, the shear stress at the channel centerline fluctuates around its mean value, resulting in fluctuations in the centerline viscosity. The simulation results will enable us to evaluate the mean viscosity at the wall, μ_w, expressed as a ratio to the reference viscosity, $\beta_w = \mu_w/\mu_0$. Consequently, the effective shear Reynolds number can be calculated as $\mathrm{Re}_{\tau,w} = \mathrm{Re}_{\tau,0}/\beta_w$. This will be instrumental in presenting the results in wall units (i.e., using μ_w).

The initial condition for the shear-thickening simulations is taken from a preliminary DNS of single-phase fully developed Newtonian turbulent channel flow at $\mathrm{Re}_\tau = 180$. Then the non-Newtonian rheology is switched on, and the specific value of the Carreau number, from Cu = 0.1 up to Cu = 10, is set. These two parameters are then fed into the Carreau model, Eq. (5), so to study the effect of a stronger shear-thickening rheology on turbulence. An illustration of this concept is shown in Fig. 3. The grid resolution has been chosen so to fulfill requirements imposed by DNS [35,36]. Compared to the Newtonian ($n = 1$) and the shear-thinning ($n < 1$) cases [20], Kolmogorov scale becomes larger with increasing shear-thickening flow index. Therefore, the resolution is chosen based on the highest Reynolds number, i.e., the reference shear Reynolds number $\mathrm{Re}_{\tau,0} = 180$, instead of the effective shear Reynolds number $\mathrm{Re}_{\tau,w}$, for all the simulations. The corresponding computational domain (whose size, as mentioned above, is $L_x \times L_y \times L_z = 16\pi h \times 4\pi h \times 2h$) has $N_x \times N_y \times N_z = 1024 \times 512 \times 129$ grid points. A summary of the simulation parameters is given in Table I. Note that for the Newtonian reference case at $\mathrm{Re}_\tau = 180$, a computational domain

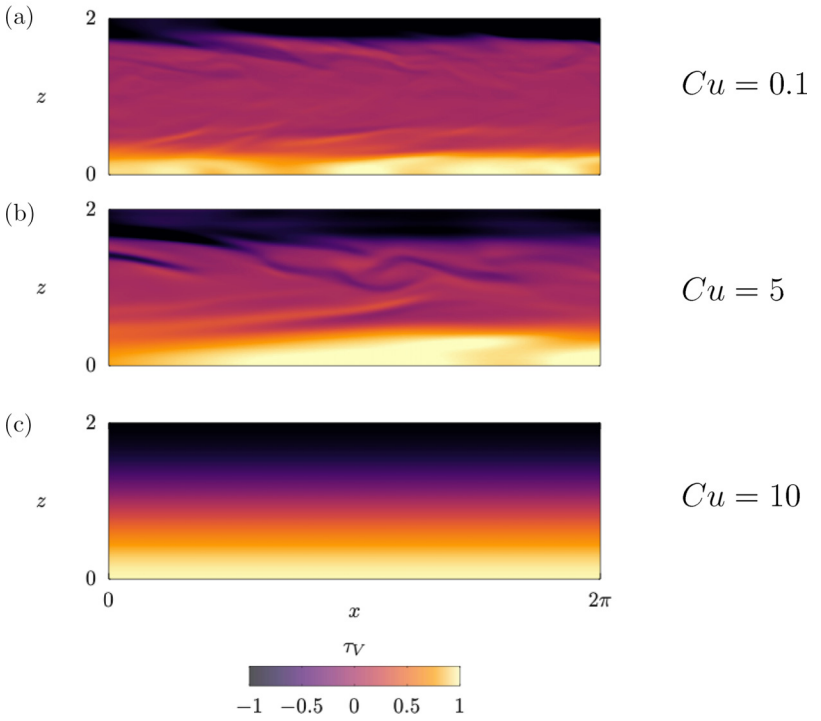

FIG. 3. Effect of Carreau number on the shear stresses distribution in the channel. The contour maps represent the viscous stress distribution, τ_V, computed as the product of the average viscosity and shear rate, for different Cu: (a) Cu = 0.1, (b) Cu = 5, and (c) Cu = 10. These outputs highlight the effect of increasing non-Newtonian intensity on the distribution and magnitude of viscous stresses, illustrating the coupling of shear-thickening behavior described by the Carreau constitutive equation and turbulence.

of size $L_x \times L_y \times L_z = 4\pi h \times 2\pi h \times 2h$ is employed and is discretized using $N_x \times N_y \times N_z = 256 \times 256 \times 129$ grid points. Simulations are considered in statistically steady conditions once the value of the bulk Reynolds number $\mathrm{Re}_{b,0}$ fluctuates about its averaged value. When this condition is met, statistics are collected.

III. RESULTS

In the present study we build on top of previous literature works [13,20] to deepen the analysis of non-Newtonian effects in wall-bounded turbulence. In particular, we will try to draw a cause-and-effect link between the Carreau number Cu, the near-wall turbulent structures and the macroscopic flow properties. To begin with, we look at the behavior of the main macroscopic flow parameters, like the volume flowrate Q and the pumping power $P = Q\Delta p$, as a function of the Carreau number Cu. Recalling that the mean pressure gradient is kept constant among all cases, P is directly proportional to Q. It is interesting to note [see Fig. 4(a)] that the behavior of P (normalized by the reference value of the power at $\mathrm{Re}_\tau = 180$) exhibits a nonmonotonic behavior as Cu increases, characterized by a gradual decrease of P in the range $0.1 < \mathrm{Cu} < 5$, followed by a sharp increase at Cu = 10. These results can be understood considering the behavior of the specific volume flowrate Q/A as a function of the effective shear Reynolds number, $\mathrm{Re}_{\tau,w}$ (listed also in Table I), as shown in Fig. 4(b). The shear-thickening cases at Cu = 0.1, Cu = 1, and Cu = 5 have, respectively, $\mathrm{Re}_{\tau,w} = 111$, $\mathrm{Re}_{\tau,w} = 76$, and $\mathrm{Re}_{\tau,w} = 58$. As highlighted by their Q-$\mathrm{Re}_{\tau,w}$ relationship following a

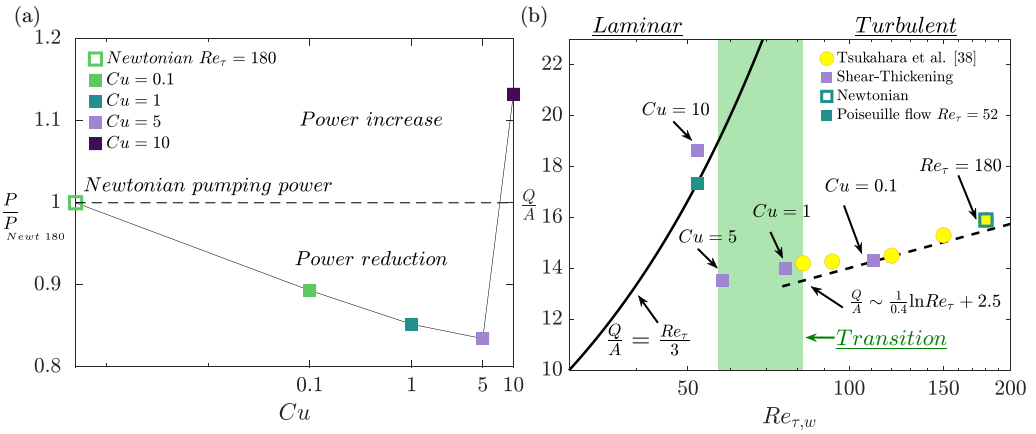

FIG. 4. Influence of increasing shear-thickening rheology on the main macroscopic flow properties. (a) Pumping power injected into the flow for the different cases, normalized by the value of the pumping power of the Newtonian case at $\mathrm{Re}_\tau = 180$. Note that the mean pressure gradient is kept constant among all cases. (b) Flow rates normalized by the area, Q/A, against the effective shear Reynolds number $\mathrm{Re}_{\tau,w}$ for all cases presented in this work (see Table I). The Newtonian results from Tsukahara *et al.* [38] and the analytical Newtonian Poiseuille flow case at $\mathrm{Re}_\tau = 52$ (corresponding to the shear-thickening case at $\mathrm{Cu} = 10$) are also included.

turbulent Newtonian-like trend (dashed line), these cases behave as non-Newtonian turbulent flows. At $\mathrm{Cu} = 10$, the situation is different, and the flow has a laminar-like behavior. This seems to suggest the tendency for the shear-thickening rheology to broaden the turbulent regime, down to values of Re_τ for which a Newtonian flow would be laminar [see green area in Fig. 4(b)] [37–39]. There is indeed firm evidence that a laminar channel flow is linearly stable up to a critical bulk Reynolds number $\mathrm{Re}_b = 790$ [37], or alternatively, down to a critical shear Reynolds number $60 < \mathrm{Re}_{\tau,c} < 64$ [38,39]. Note also that this value is in any case much lower than the one that can be predicted via stability analysis of plane Poiseuille flow for Newtonian fluids [37].

A. Qualitative behavior of the flow fields

We now look at the qualitative structure of the flow in the statistically steady regime. Figure 5 shows the contour map of the instantaneous streamwise velocity u^+ for different Carreau numbers on a wall-parallel $(x - y)$ section of the channel located at $z^+ = 10$, where the maximum of the integral length scale l_x, i.e., the maximum velocity correlation, occurs [14]. As indicated by the corresponding label, each panel refers to a different case. The reference Newtonian case at $\mathrm{Re}_\tau = 180$ is also shown [Fig. 5(a)] for comparison purposes. Note that the simulation at $\mathrm{Cu} = 10$, ending up into a laminar state, is not shown. In the Newtonian case [Fig. 5(a)], the classic near-wall turbulence structure, characterized by elongated high- and low-velocity streaks arranged side by side and lined up along the streamwise flow direction is recovered [40,41]. Together with the longitudinal quasi-streamwise vortices that populate the near wall region, they form the near-wall regeneration cycle and represent a major contribution to the production of the turbulent kinetic energy (TKE) [42–44]. With increasing shear-thickening rheology, $\mathrm{Cu} > 0$ [shown in Figs. 5(b)–5(d)], we observe that the near-wall velocity streaks become progressively longer in the streamwise direction and thicker in the spanwise direction. The longer and thicker velocity streaks are associated with a reduced activity of near wall vortices and therefore a reduced activity of sweeps/ejections (whose primary effect is to transfer energy and momentum in the wall-normal direction [35,43,45]). The reason for this behavior, as will be explained in detail later, is that, by keeping the mean pressure gradient constant, a shear-thickening fluid has a viscosity that increases with shear, i.e., it is

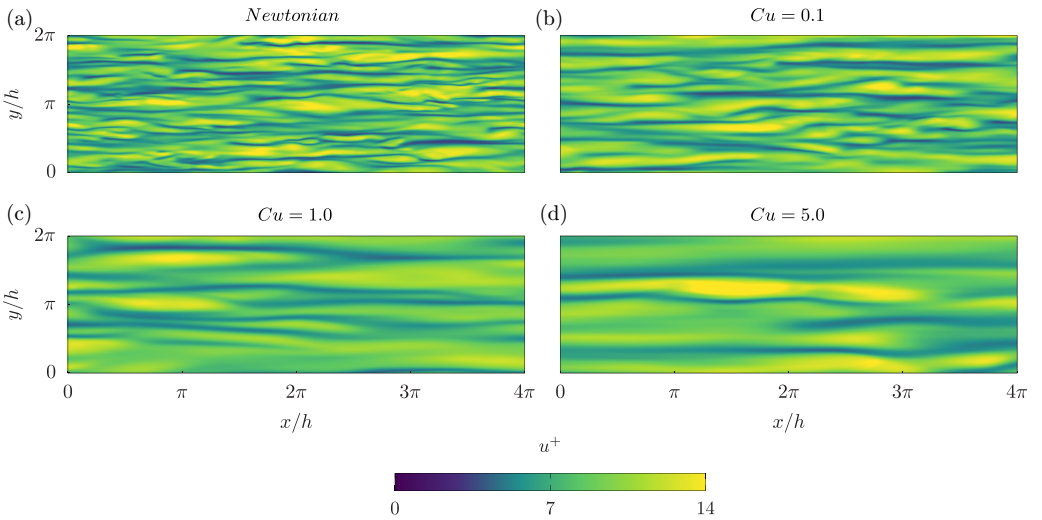

FIG. 5. Instantaneous contours of the streamwise velocity in the $\langle x - y \rangle$ plane at $z^+ = 10$ from the bottom wall. Results are shown for the different cases for increasing non-Newtonian intensity: (a) Newtonian case at $\mathrm{Re}_\tau = 180$; (b) shear-thickening case at $\mathrm{Cu} = 0.1$; (c) shear-thickening case at $\mathrm{Cu} = 1$; and (d) shear-thickening case at $\mathrm{Cu} = 5$. Note that the shear-thickening case at $\mathrm{Cu} = 10$ is not shown, since it achieves laminar conditions.

characterized by a larger viscosity near the wall (where the shear is indeed larger). This induces the turbulence reduction, which can also lead to a full laminarization of the flow (observed in the present case for $5 < \mathrm{Cu} < 10$).

We now turn our attention to the distribution of u^+ on a horizontal $\langle x - y \rangle$ plane between the bottom wall and the centerline, located at distance $z = -0.5$. Results are shown in Fig. 6. A trend similar to the one described above is observed. Increasing the non-Newtonian rheology, i.e., increasing Cu, reduces the turbulence activity. In particular, Figs. 5(d) and 6(d) ($\mathrm{Cu} = 5$ case) provides a clear representation of the coexistence between laminar and turbulent patches (this coexistence disappears at $\mathrm{Cu} = 10$, when the flow is fully laminar).

B. Mean flow statistics

The effect of the Carreau number Cu on the mean velocity profile $\overline{u}$ is shown in Figs. 7(a) and 7(b) in linear and semilogarithmic scale, respectively. Note that outer units are used for the wall-distance coordinate axis z in Fig. 7(a), while inner units are used in Fig. 7(b).We consider first Fig. 7(a), where the wall-normal distance is expressed in outer units as $z = z^+/\mathrm{Re}_{\tau,w} - 1$. We immediately notice that the velocity gradients at the wall, $\partial\overline{u}/\partial z|_w$, reduce for increasing Cu. This can be understood considering that, for shear-thickening fluids, the apparent viscosity is larger near the wall (where the shear is larger). Recalling that the mean pressure gradient $\nabla\overline{p}$ that drives the flow is kept constant among cases, a larger near wall viscosity would induce a smaller strain rate (i.e., velocity gradient) at the wall, so to keep the balance between the force applied by the pressure gradient and the resistance exerted by the shear stress. The decrease of the velocity gradient at the wall induces a corresponding decrease of the effective shear Reynolds number $\mathrm{Re}_{\tau,w}$ (see also values in Table I). We observe that, for shear-thickening fluids up to $\mathrm{Cu} = 5$, the velocity profile follows the behavior of turbulent low-Re flows, with a flow rate Q that, compared to the Newtonian case, reduces for increasing Cu (i.e., drag increase effect). At $\mathrm{Cu} = 10$ (solid purple line), the shear-thickening effect is so pronounced, and the apparent viscosity at the wall so large, that the corresponding strain rate falls below the critical value required to sustain a turbulent flow, and the flow becomes laminar. This reflects into a

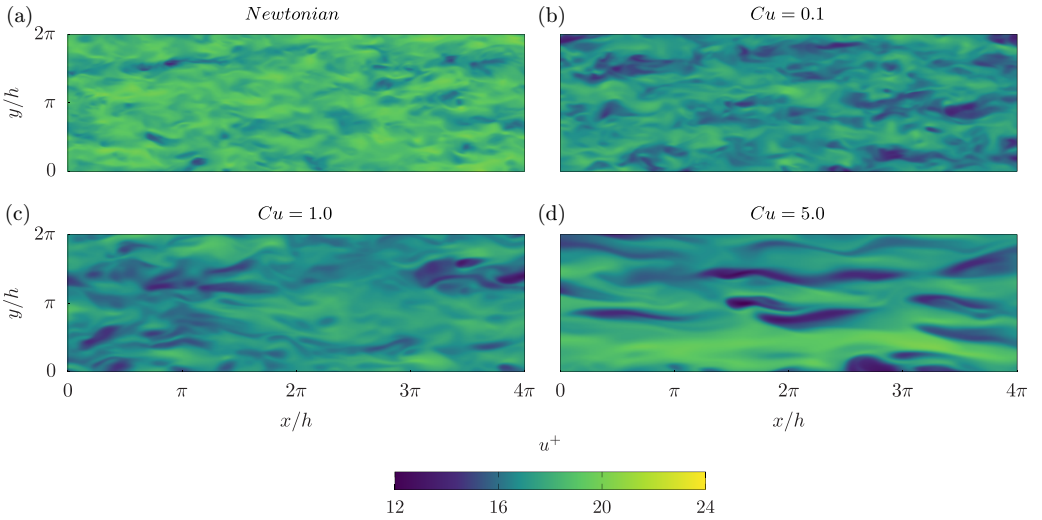

FIG. 6. Contour maps of the streamwise velocity in the $\langle x-y\rangle$ plane at $z=-0.5$ (in the outer layer) from the bottom wall. Results are shown for the different cases for increasing non-Newtonian intensity: (a) Newtonian at $\mathrm{Re}_\tau = 180$; and consequently for the shear-thickening flows (b) $\mathrm{Cu} = 0.1$ at $\mathrm{Re}_{\tau,w} = 111$; (c) $\mathrm{Cu} = 1$ at $\mathrm{Re}_{\tau,w} = 76$ and (d) $\mathrm{Cu} = 5$ at $\mathrm{Re}_{\tau,w} = 58$. Note that the shear-thickening case at $\mathrm{Cu} = 10$ is not shown, since it is laminar.

parabolic-like velocity profile. The velocity profile of the laminar Newtonian analytical case at the same effective Reynolds number $\mathrm{Re}_{\tau,w} = 52$ (purple dashed curve) is also shown for comparison purposes. Interestingly, case $\mathrm{Cu} = 10$ exhibits larger values of the mean velocity near the channel center compared to the corresponding Newtonian profile. Indeed, although both flows are laminar, in the non-Newtonian case the mean viscosity over the whole domain is smaller than the wall viscosity, due to the shear-thickening behavior. This cause the flow velocity of the non-Newtonian case to be larger than the corresponding Newtonian one. To deepen our analysis, we look at the flow velocity

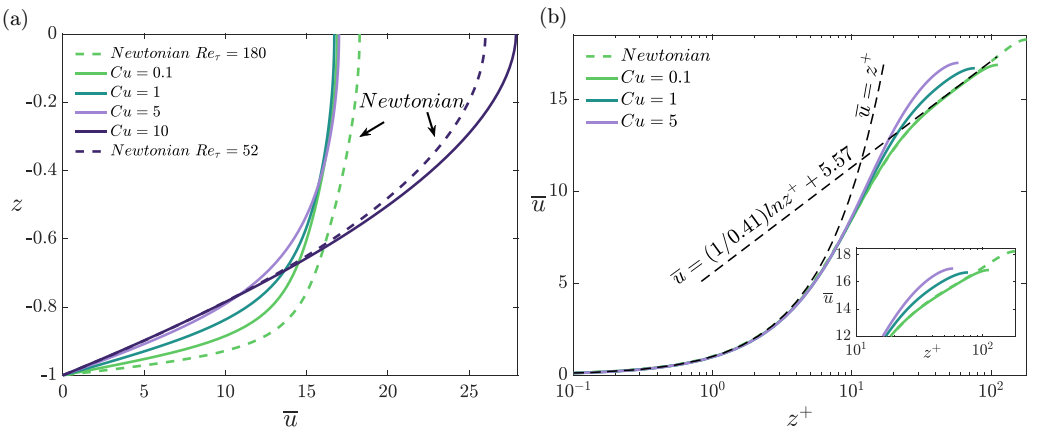

FIG. 7. Mean streamwise velocity profiles $\overline{u}$ as a function of the distance from the wall. The different shear-thickening cases considered are shown as solid lines. The Newtonian cases at $\mathrm{Re}_\tau = 180$ and $\mathrm{Re}_\tau = 52$ (respectively in light green and purple dashed lines) are also shown for reference. In (a) all the turbulent cases are expressed in outer units, $z = z^+/\mathrm{Re}_{\tau,w} - 1$, whereas in (b) wall units z^+ are adopted.

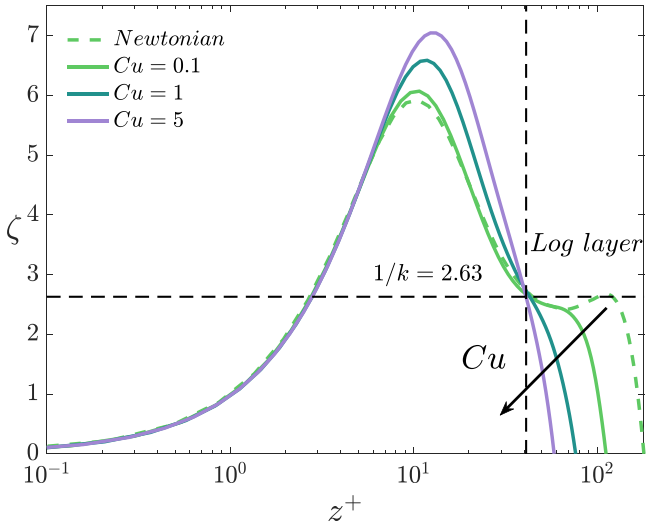

FIG. 8. Velocity diagnosis function, $\zeta = z^+ d\overline{u}^+/dz^+$. Results are shown in wall units z^+, for the turbulent shear-thickening rheologies at different Carreau numbers Cu. The Newtonian case at $\mathrm{Re}_\tau = 180$ is also shown.

in inner units; see Fig. 7(b). Note that the results for Cu = 10 is not shown, because the flow is laminar in this condition, and plotting its behavior would reduce the readability of the other results. While in the near-wall region ($z^+ < 10$) velocity profiles collapse on top of each other, away from the wall they are different. For the Newtonian case at $\mathrm{Re}_\tau = 180$ (dashed green line) the law of the wall is closely recovered. For the non-Newtonian cases (solid lines) the situation is different. For Cu = 0.1, the behavior is similar to the one of the Newtonian case, though the extension of the log-layer region is shorter (solid green line). For increasing Cu, the velocity profiles at $z^+ > 10$ do depart from the law of the wall and become larger, trespassing the Newtonian behavior and not following a clear logarithmic behavior. Linked to the discussion on the flow velocity, we now focus on the diagnosis velocity function, $\zeta = z^+ d\overline{u}/dz^+$, which is shown in Fig. 8. Based on the behavior of ζ it is possible to identify the main flow regions of the channel: the viscous sublayer (region near the wall, typically up to $z^+ \simeq 5$), the logarithmic layer (region away from the wall, where ζ is approximately constant), and the buffer layer (region in between the viscous and the logarithmic layer). Note that the point where ζ is maximum, $z_{\zeta,\max}$, identifies the point in the buffer layer where viscous effects are balanced by inertial effects. We first consider the Newtonian case, the green dashed line. We notice that the point of maximum is around $z^+_{\zeta,\max} \simeq 10$, while the logarithmic layer sets in when $\zeta = z^+ \partial\overline{u}/\partial z^+ = 1/k = 2.63$ (explicitly indicated by the horizontal dashed line), i.e., around $z^+ \simeq 40$. Unfortunately, because of the low Reynolds number of the present simulations, the log layer does not seem very robust. There is only a short region where ζ is approximately constant, $40 < z^+ < 140$. We consider now the influence of the non-Newtonian rheology. As expected all profiles collapse in the viscous sublayer, given the linear behavior of the velocity as a function of z^+ (see also Fig. 7). However, they do have different behaviors in the buffer and logarithmic layers. In particular, we notice that, for increasing Cu, the maximum of ζ increases and is shifted farther away from the wall. This indicates the predominance of viscous effects over inertial ones up to a larger distance from the wall. At the same time, for increasing Cu, the logarithmic layer tends to disappear completely (see the absence of an horizontal plateau of ζ for the non-Newtonian cases). Altogether, these observations indicate that the viscous effects become more and more important over inertia, to the point that the flow tends to laminarize (which indeed happens for Cu = 10, not shown in the picture).

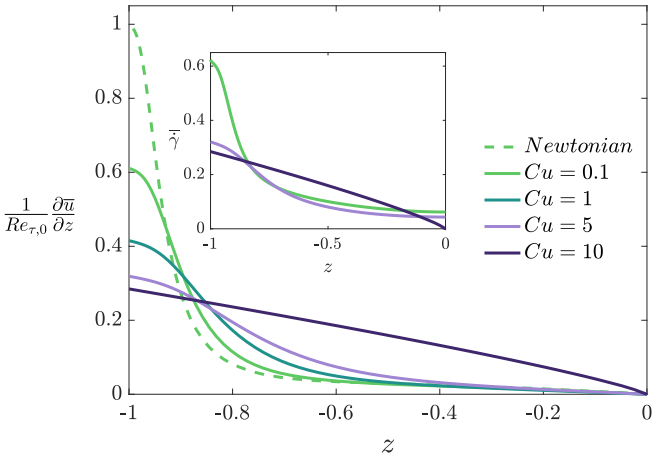

FIG. 9. Main axial shear rate $1/\mathrm{Re}_{\tau,0}\partial\overline{u}/\partial z$ as a function of the outer wall-normal coordinate z for all cases. The inset highlights the mean strain rate $\overline{\dot{\gamma}}$ profiles for the transitional cases (Cu $= 0.1$ and Cu $= 5$) and the laminar case marked by Cu $= 10$, illustrating fluid deformation progression from weak to strong shear-thickening behavior. Dashed lines represent Newtonian reference cases, while solid lines show shear-thickening fluids with increasing Cu.

Given its importance in the rheological properties of the fluid, it is now interesting to focus on the shear rate (and more in general on the strain rate). This is considered in Fig. 9. In particular, we plot the behavior of the main axial shear rate $1/\mathrm{Re}_{\tau,\mathrm{ref}}\partial\overline{u}/\partial z$, while in the inset we represent the behavior of the mean strain rate

$$\overline{\dot{\gamma}} = \frac{1}{\mathrm{Re}_{\tau,0}}\overline{\sqrt{2\mathbf{S}\mathbf{S}}} = \frac{1}{\mathrm{Re}_{\tau,0}}\overline{\left[2\left(\frac{\partial u}{\partial x}\right)^2+2\left(\frac{\partial v}{\partial y}\right)^2+2\left(\frac{\partial w}{\partial z}\right)^2+\left(\frac{\partial u}{\partial y}+\frac{\partial v}{\partial x}\right)^2+\left(\frac{\partial u}{\partial z}+\frac{\partial w}{\partial x}\right)^2+\left(\frac{\partial v}{\partial z}+\frac{\partial w}{\partial y}\right)^2\right]^{\frac{1}{2}}} \tag{9}$$

for the transitional cases (Cu $= 0.1$ and Cu $= 5$) and for the laminar one (Cu $= 10$). Since the expression of $\dot{\gamma}$ cannot be further simplified—due to the three-dimensional nature of the turbulent flow field—it is not possible to assume that the strain rate is equal to the shear rate, $\overline{\dot{\gamma}} \neq \partial\overline{u}/\partial z$. Considering Fig. 9, we notice that the main axial shear rate is maximum at the wall and then decays until it reaches the center of the channel where, due to flow symmetry, $\partial\overline{u}/\partial z = 0$. We also observe that Cu affects $\partial\overline{u}/\partial z$ in two ways. Compared to the Newtonian case, increasing Cu reduces $\partial\overline{u}/\partial z$ near the wall, $z < -0.9$ (the slope of the mean velocity, as discussed in Fig. 7), but increases the shear rate away from the wall, $z > -0.9$. For Cu $= 10$, the flow is laminar, and $\partial\overline{u}/\partial z$ is linear. In fact, $\partial\overline{u}/\partial z = \overline{\tau}\mathrm{Re}_{\tau,\mathrm{ref}}/\beta$ is nonlinear since β is a function of the strain rate. We now consider the behavior of $\overline{\dot{\gamma}}$. From a comparison between the two relevant quantities, we notice that $\partial\overline{u}/\partial z$ and $\overline{\dot{\gamma}}$ are similar near the wall, up to $z \simeq -0.85$. This similarity exists because the magnitude of the fluctuating components of the shear rate tensor $\mathbf{S}w'$ is smaller than the mean $\overline{\mathbf{S}}w$, with the only nonzero component being in the wall normal direction. This similarity does not hold in the core of the channel, where the influence of turbulence makes the contribution of the nonaxial components important. Differently from what noticed for $\partial\overline{u}/\partial z$, the influence of Cu is very important near the wall ($z < -0.9$), but it reduces elsewhere. However, an interesting observation is to be made here. Away form the wall, an increase of Cu results in an increase of $\partial\overline{u}/\partial z$, while at the same time it induces a decrease of $\overline{\dot{\gamma}}$ (but for the case Cu $= 10$, which is, however, in a laminar condition). In other terms, Cu acts to decrease the fluid deformation at the core of the channel. The

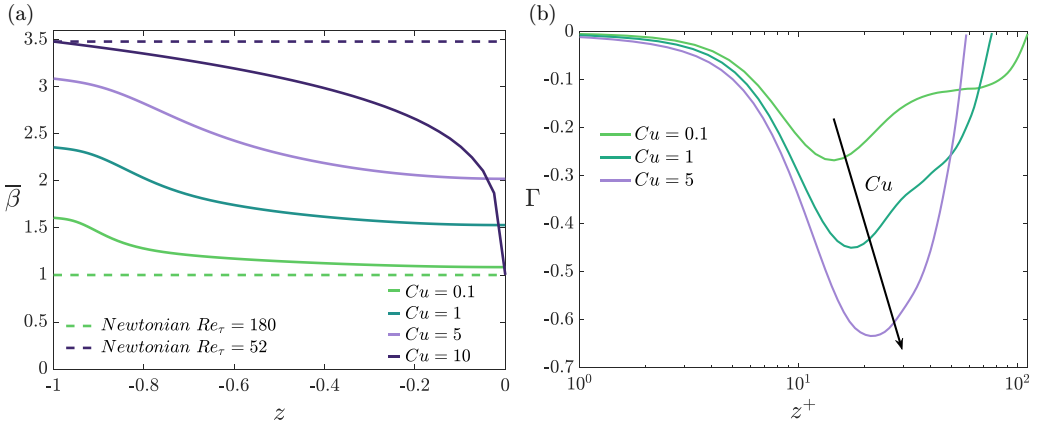

FIG. 10. Shear-thickening effect on viscosity distributions. (a) Profiles of the normalized viscosity $\overline{\beta} = \overline{\mu}/\mu_0$, based on the zero strain rate viscosity μ_0, in outer units and (b) its relative viscosity diagnosis function $\Gamma = z^+ d\overline{\beta}/dz^+$ in wall units.

different behavior emerges because the strain rate incorporates all turbulent fluctuations effects on deformation, in which nonaxial components become more important in the turbulent core.

Figure 10 illustrates the key role of viscosity distribution in the fluid dynamics of non-Newtonian flows. The normalized mean viscosity profiles $\overline{\beta} = \overline{\mu}/\mu_0$, sketched in Fig. 10(a), show a strong dependence on the Carreau number Cu. In particular, all the shear-thickening cases are characterized by a mean viscosity $\overline{\beta}$ that decreases monotonically from the value at the wall, towards the value at the channel center. This is due to the decrease of the strain rate (and hence of the viscosity; see the rheology map in Fig. 2) going from the wall to the channel center (see Fig. 9). By keeping constant the mean pressure gradient $\nabla\overline{p}$, the flow index n, and the extreme viscosity values (μ_0, μ_∞), we notice that as Cu increases, the curves are forced to assume higher viscosity values (higher viscosity at higher shear rates, i.e., at the wall.). The increase in the mean viscosity at the wall, $\overline{\beta}_w = \overline{\beta}|_{z=-1}$ effectively reduces the shear Reynolds number $\mathrm{Re}_{\tau,w}$ and is therefore the main cause of the transition from turbulent to laminar flow. It is also important to consider that the condition $\overline{\beta} = 1$ inside the channel is only reached for the laminar case $\mathrm{Cu} = 10$, for which the strain rate becomes zero $\dot{\gamma}|_{z=0} = \partial\overline{u}/\partial z|_{z=0} = 0$ [while it is not the case for the other simulations; see Fig. 9(b)]. The diagnosis function $\Gamma = z^+ d\overline{\beta}/dz^+$, shown in Fig. 10(b), reveals key trends. Minima $\Gamma_{\min}$ indicate that after a constant viscosity region, $\overline{\beta}$ first decreases sharply and then more gradually. Profiles show that a logarithmic region for $\overline{\beta}$ (constant Γ) can form but narrows as Cu increases, being visible only for $\mathrm{Cu} = 0.1$. As Cu increases, the peak magnitude rises (indicating larger $\overline{\beta}$ gradients), and the peak shifts away from the wall. This trend aligns with the diagnosis velocity function ζ (Fig. 8), which shows that higher Cu widens the viscous layer and diminishes the log layer, signaling flow relaminarization. From Γ, we see why turbulence persists for $\mathrm{Cu} = 5$: increasing Cu reduces mean viscosity outside the viscous layer, which can sustain turbulence. In summary, a higher Cu generally dampens turbulence but also causes more significant viscosity reductions, thereby delaying relaminarization. The balance between these effects determines whether full laminarization occurs.

C. Stress budget and higher order turbulent flow statistics

The total mean shear stress $\overline{\tau} = \overline{\tau}^+/\tau_w$ for a statistically stationary fully developed channel flow of a generalized Newtonian (GN) fluid can be obtained applying Reynolds decomposition to Eq. (6). Considering the nature of the problem at hand, in addition to the velocity $\mathbf{u} = \overline{\mathbf{u}} + \mathbf{u}'$ and the pressure $p = \overline{p} + p'$ also the nondimensional viscosity $\beta = \overline{\beta} + \beta'$ and the strain rate tensor $\mathbf{S} = \overline{\mathbf{S}} + \mathbf{S}'$ are decomposed. The resulting nondimensional total shear stress $\overline{\tau}^+$ (where the

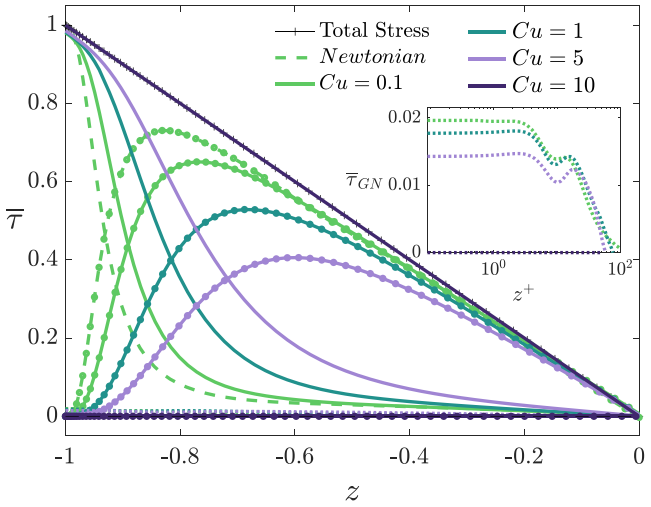

FIG. 11. Influence of the Carreau number Cu on the mean shear stress budget as a function of the wall normal distance. Viscous stresses are identified by solid lines while turbulent stresses are identified by lines with circles. Note that the pressure gradient $\nabla\overline{p}$ among the cases is kept constant, i.e., constant τ_w. The top right inset shows the influence of increasing shear-thickening rheology on the generalized-Newtonian $\overline{\tau}_{GN}$ stresses, shown in dotted lines, in proximity of the wall (with wall-normal distance expressed in wall units).

superscript + will be dropped for ease of reading) is linear and can be expressed as

$$\overline{\tau} = \overline{\tau}_V + \overline{\tau}_T + \overline{\tau}_{GN} = 1 - \frac{z^+}{\mathrm{Re}_{\tau,w}}, \tag{10}$$

which can be thought as the sum of a viscous stress,

$$\overline{\tau}_V = \frac{\overline{\beta}}{\mathrm{Re}_{\tau,0}} \frac{\partial \overline{u}}{\partial z}, \tag{11}$$

a turbulent stress $\overline{\tau}_T = -\overline{u'w'}$, and a generalized Newtonian stress,

$$\overline{\tau}_{GN} = \frac{1}{\mathrm{Re}_{\tau,0}} \overline{\beta' \left(\frac{\partial u'}{\partial z} + \frac{\partial w'}{\partial x} \right)}, \tag{12}$$

also called turbulent viscous stress, which takes into account the non-Newtonian effects due to the coupling with turbulence. The non-Newtonian stress plays a role similar to that of polymer stress in a viscoelastic fluid [46,47]. While in a viscoelastic fluid polymer elasticity mechanically interacts with coherent turbulence structures, in a GN fluid, this role is assumed by the combined effects of viscosity and shear rate fluctuations [13]. In particular, the shear-thickening rheology cause this stress to assume positive values, since a fluctuation in shear rate $(\partial u/\partial z)' + (\partial w/\partial x)'$ induces an alike fluctuation (same sign) in viscosity β'. The behavior of the total stress, as well as its components Eqs. (10)–(12), is shown in Fig. 11 for the different cases considered in this study. As expected, no matter the value of Cu, the total stress is linear with z (symbols), since the mean pressure gradient, is kept constant for all cases. Looking now at the behavior of the viscous stress, $\overline{\tau}_V$, we note that it is maximum at the wall ($z = -1$), with a value slightly smaller than unity (because of shear thickening), and then decreases monotonically moving away from the wall until reaching the 0 value at the channel center ($z = 0$). For increasing Cu, we notice an increase of $\overline{\tau}_V$. The behavior of the turbulent stress component, $\overline{\tau}_T$, complements that of $\overline{\tau}_V$, as required by the total stress budget. The turbulent stress, $\overline{\tau}_T$, is zero at the wall ($z = -1$), peaks in the buffer

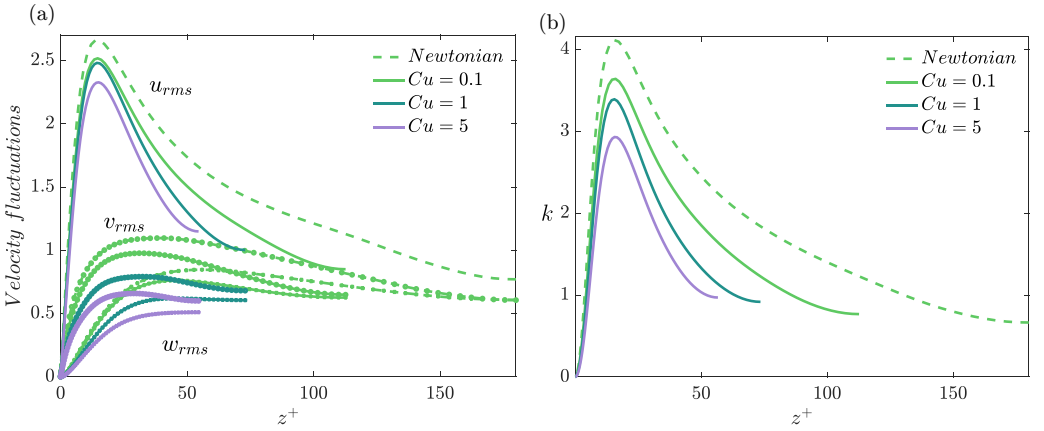

FIG. 12. Profiles of the velocity root-mean-square intensities (with u, v, and w components shown in solid, dashed, and dotted lines, respectively) as a function of wall-normal location in wall units (a), along with the turbulent kinetic energy k (b).

layer, and then decreases to zero at the channel center ($z = 0$). As Cu increases, the peak moves away from the wall (from $z_{\max} \simeq 0.85$ for the Newtonian case to $z_{\max} \simeq 0.6$ for Cu $= 5$), and its magnitude decreases from $\overline{\tau}_{T,\max} \simeq 0.75$ (Newtonian) to $\overline{\tau}_{T,\max} \simeq 0.4$ (Cu $= 5$). The decrease in $\overline{\tau}_T$ by 40% for Cu $= 5$ is notable, considering the effective shear Reynolds number $\mathrm{Re}_{\tau,w} = 58$ (below the critical Newtonian $\mathrm{Re}_{\tau,c}$), yet turbulence is sustained. This behavior results from the complete elimination of the logarithmic layer [Fig. 7(b)] and the stronger viscosity decrease in the buffer layer [48]. The reduction in $\overline{\tau}_T$ with increasing Cu reflects a reduced turbulence activity (and $\mathrm{Re}_{\tau,w}$). For Cu $= 10$, $\overline{\tau}_T = 0$ and $\overline{\tau}_V = \overline{\tau}$, indicating full laminarization. Fig. 11 shows that the importance of $\overline{\tau}_{GN}$ is limited to the near-wall region. The inset of Fig. 11 plots $\overline{\tau}_{GN}$ in semilogarithmic scale. $\overline{\tau}_{GN}$ is maximum and constant in the viscous sublayer ($z^+ < 5$), fluctuates in the buffer layer around $z^+ = 10$, and decreases to zero at the channel center. As Cu increases, non-Newtonian stresses become smaller, and the local minimum/maximum shift away from the wall. The behavior of the root mean square of the velocity fluctuations in the streamwise, u_{rms}, spanwise, v_{rms}, and wall-normal fluctuations, w_{rms}, is shown in Fig. 12. Results from the reference Newtonian simulation are shown by the dashed line, while results from the non-Newtonian simulations are shown by solid lines. We clearly observe that, compared to the Newtonian case, all three components of the velocity fluctuations reduce in magnitude, as a direct consequence of the progressively stronger laminarization process. This trend is also confirmed by the behavior of the turbulent kinetic energy, $k = 1/2\overline{\mathbf{u}}' \cdot \mathbf{u}' = \mathbf{u}_{\mathrm{rms}} = 1/2(u_{\mathrm{rms}}^2 + v_{\mathrm{rms}}^2 + w_{\mathrm{rms}}^2)$, shown in Fig. 12(b). It is interesting to observe that, by keeping the zero strain rate viscosity constant among the simulations (imposed by keeping the same reference Reynolds number $\mathrm{Re}_{\tau,0} = 180$ based on the pressure gradient), the curves tend to assume the same levels of turbulence intensity at the channel centerline (whose location changes, when plotted in local wall units). Further insights into the flow structure can be gained by analyzing the streamwise root mean square of the vorticity, defined as

$$\omega_{x,\mathrm{rms}} = \overline{\omega_x'^2}^{\frac{1}{2}} = \frac{1}{\mathrm{Re}_{\tau,0}} \overline{\left(\frac{\partial w'}{\partial y} - \frac{\partial v'}{\partial z} \right)^2}^{\frac{1}{2}} \tag{13}$$

and shown in Fig. 13. Reportedly [35], the (relative) minimum and maximum values of the root-mean-square velocity, $\min(\omega_{x,\mathrm{rms}})$ and $\max(\omega_{x,\mathrm{rms}})$, respectively, correspond to the mean locations of the vortex edge and center, respectively. Results (see inset of Fig. 13) indicate that the size of the average vortices tends to be reduced and shifted closer to the wall by the non-Newtonian rheology. The reduced vortical sizes and their simultaneous shift toward the wall collectively

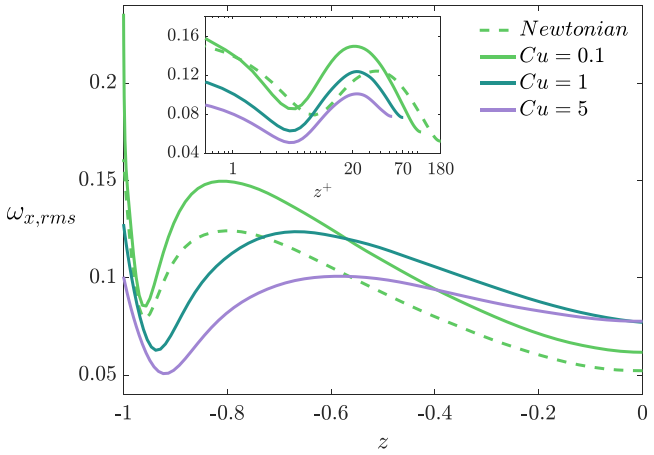

FIG. 13. Vorticity root mean square $\omega_{x,\mathrm{rms}}$ as a function of the wall-normal location in outer units (main panel) and in wall units and semilog scale (inset).

indicate the formation of more constrained vortical structures. Consequently, the shear-thickening effects essentially confine the vortices to a narrower region closer to the wall compared to the Newtonian case.

We finally focus a bit further on the generalized Newtonian stress, $\overline{\tau}_{GN}$, which develops in case of non-Newtonian rheology. Given the expression $\overline{\tau}_{GN} = 1/\mathrm{Re}_{\tau,\mathrm{ref}}\overline{\beta'((\partial u/\partial z)' + (\partial w/\partial x)')}$, it seems instrumental to look at the behavior of the root mean square of the strain rate, $\dot{\gamma}_{\mathrm{rms}}$, and of the viscosity, β_{rms}, which represent the building blocks of $\overline{\tau}_{GN}$. This is done in Fig. 14. From the combined analysis of Figs. 14(a) and 14(b), it is apparent that the larger values of $\overline{\tau}_{GN}$ (see Fig. 11) stems from the non-negligible values of $\dot{\gamma}_{\mathrm{rms}}$ and β_{rms}, in particular in the near-wall region. Larger values of β_{rms} are observed at larger Cu, seemingly in contrast with the observed flow phenomenology (i.e., the tendency to laminarize for increasing Cu). This is a direct consequence of the increased mean value of $\overline{\beta}$ for increasing Cu, which, in combination with nonvanishing velocity fluctuations, gives higher values of β_{rms}. Indeed, we notice that, while in the viscous layer

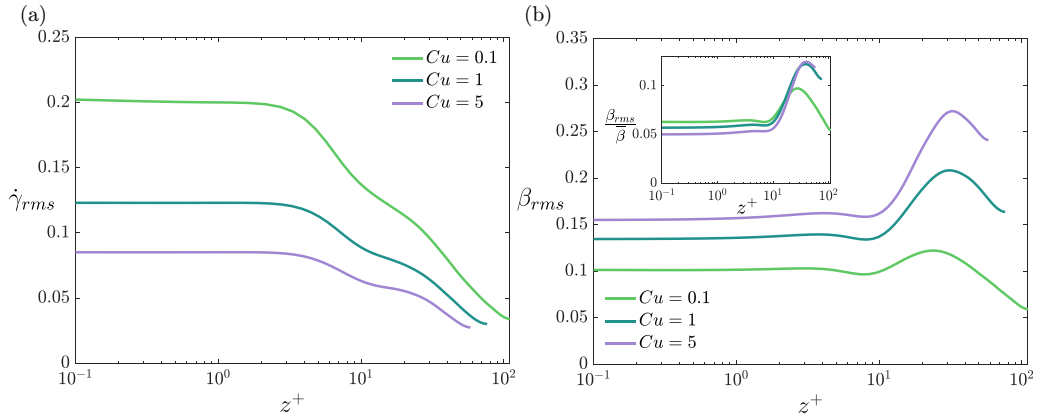

FIG. 14. Second-order turbulent intensities related to the non Newtonian stress $\overline{\tau}_{GN}$. (a) strain rate root mean square $\dot{\gamma}_{\mathrm{rms}}$ and (b) viscosity root mean square β_{rms} over the wall normal direction z^+ in wall units. The inset shows the viscosity root mean square $\beta_{\mathrm{rms}}/\overline{\beta}$ compensated with the mean viscosity over the wall normal direction z^+ in wall units.

($z^+ < 10$) $\beta_{\text{rms}}/\overline{\beta}$, shown as an inset of Fig. 14(b), is approximately constant and independent of Cu, outside the viscous layer $\beta_{\text{rms}}/\overline{\beta}$ increases with Cu. This seems to support the idea that the increased viscosity fluctuations are mostly due the turbulent behavior of the strain rate. Note, however, that the increase of β_{rms} for increasing Cu is more than compensated by the decrease of $\dot{\gamma}_{\text{rms}}$ (for increasing Cu), finally giving a $\overline{\tau}_{GN}$ that decreases with increasing Cu (see Fig. 11). It is also interesting to observe that the nonmonotonic behavior of $\overline{\tau}_{GN}$, with the development of a local maximum in the buffer region (see Fig. 11), is a direct consequence of the nonmonotonic behavior of β_{rms}, which displays a similar local maximum therein ($z^+ \simeq 30-40$).

IV. CONCLUSIONS

In this work, we conducted direct numerical simulations of turbulent channel flow for a continuous shear-thickening fluid modeled using the Carreau constitutive equation. The non-Newtonian flow behavior was examined under an imposed mean pressure gradient for various Carreau numbers, Cu, representing the fluid characteristic timescale.

Our analysis of first-order statistics revealed that shear-thickening rheology causes a marked reduction in mean viscosity with increasing distance from the wall. This rheological effect modifies the mean velocity profiles and turbulence dynamics when compared to Newtonian flow at the same shear Reynolds number. At the lowest Carreau number (Cu = 0.1), the flow exhibited a redistribution of inertial, viscous, and generalized-Newtonian forces, leading to a measurable reduction in flow rate. Qualitative analysis of flow fields demonstrated that increasing Cu suppresses turbulent structures due to enhanced near-wall viscosity. This suppression has consequences on the flow regime: at moderate Cu values the average velocity profile does not exhibit a logarithmic layer, and at higher Cu values full relaminarization is produced. A mean shear stress budget analysis revealed that changes in Cu significantly impact the balance between turbulent and viscous stresses. Specifically, turbulent stresses are redistributed in favor of viscous stresses, driven by non-Newtonian effects, which, while small in magnitude, have a pronounced impact on near-wall turbulence dynamics. Non-Newtonian stresses disrupt the self-sustaining mechanisms of turbulence by modifying the dynamics of quasi-streamwise vortices—reducing their size and population–and by broadening the longitudinal extent of velocity streaks. This leads to fewer burst events, reduced turbulent stresses, and increased stability of velocity streaks.

The Carreau number (Cu) emerges as a key parameter driving these mechanisms and promoting flow relaminarization. Simultaneously, higher Cu values lead to a pronounced reduction in mean viscosity, counteracting the relaminarizing effects of non-Newtonian stresses. The interplay between these competing effects governs the overall flow behavior. Notably, our results indicate that the viscosity reduction dominates, allowing the flow to remain turbulent even at low Reynolds numbers ($\text{Re}_\tau = 76$ and 58), where Newtonian fluids would transition to laminar flow.

ACKNOWLEDGMENTS

We acknowledge the EuroHPC Joint Undertaking for awarding this project access to the EuroHPC supercomputer LUMI, hosted by CSC (Finland) and the LUMI consortium through a EuroHPC Regular Access call (EHPC-REG-2022R01-020). The authors acknowledge the TU Wien University Library for financial support through its Open Access Funding Program. Open access funding was provided by TU Wien (TUW).

The authors report no conflict of interest.

DATA AVAILABILITY

The data that support the findings of this article are openly available [49].

[1] S. Liu and J. H. Masliyah, On non-Newtonian fluid flow in ducts and porous media, Chem. Eng. Sci. **53**, 1175 (1998).
[2] R. P Chhabra and J. F. Richardson, *Non-Newtonian Flow in the Process Industries: Fundamentals and Engineering Applications* (Butterworth-Heinemann, Oxford, 1999).
[3] S. Lee and N. D. Spencer, Sweet, hairy, soft, and slippery, Science **319**, 575 (2008).
[4] S. Ghosh, D. Choudhury, N. S. Das, and B. Pingguan-Murphy, Tribological role of synovial fluid compositions on artificial joints—A systematic review of the last 10 years, Lubr. Sci. **26**, 387 (2014).
[5] A. Sarkar, S. Zhang, M. Holmes, and R. Ettelaie, Colloidal aspects of digestion of Pickering emulsions: Experiments and theoretical models of lipid digestion kinetics, Adv. Colloid Interface Sci. **263**, 195 (2019).
[6] R. P. Chhabra, Non-Newtonian fluids: An introduction, in *Rheology of Complex Fluids* (Springer, New York, NY, 2010), pp. 3–34.
[7] R. P. Chhabra and J. F. Richardson, *Non-Newtonian Flow and Applied Rheology: Engineering Applications* (Butterworth-Heinemann, 2011).
[8] A. B. Metzner, Rheology of suspensions in polymeric liquids, J. Rheol. **29**, 739 (1985).
[9] J. F. Morris, Shear thickening of concentrated suspensions: Recent developments and relation to other phenomena, Annu. Rev. Fluid Mech. **52**, 121 (2020).
[10] R. B. Bird, R. C. Armstrong, and O. Hassager, *Dynamics of Polymeric Fiquids. Vol. 1: Fluid Mechanics* (John Wiley and Sons, New York, 1987).
[11] H. Freundlich and H. L. Röder, Dilatancy and its relation to thixotropy, Trans. Faraday Soc. **34**, 308 (1938).
[12] M. Wei, K. Lin, and L. Sun, Shear thickening fluids and their applications, Mater. Des. **216**, 110570 (2022).
[13] A. Arosemena, R. Andersson, and J. Solsvik, Turbulent channel flow of generalized Newtonian fluids at a low Reynolds number, J. Fluid Mech. **908**, A43 (2021).
[14] J. Singh, M. Rudman, and H. M. Blackburn, The influence of shear-dependent rheology on turbulent pipe flow, J. Fluid Mech. **822**, 848 (2017).
[15] M. R. Sheikhi, M. A. Sofuoğlu, and Z. Chen, *Shear Thickening Fluid Integrated Sandwich Structures for Vibration Isolation* (Springer International Publishing, Cham, 2023), pp. 27–40.
[16] M. P. Ribeiro, P. H. P. M. da Silveira, F. de Oliveira Braga, and S. N. Monteiro, Fabric impregnation with shear thickening fluid for ballistic armor polymer composites: An updated overview, Polymers **14**, 4357 (2022).
[17] E. Blanco, D. Hodgson, M. Hermes, R. Besseling, G. L. Hunter, P. M. Chaikin, M. E. Cates, E. Michael, I. Van Damme, and W. C. K. Poon, Conching chocolate is a prototypical transition from frictionally jammed solid to flowable suspension with maximal solid content, Proc. Natl. Acad. Sci. USA **116**, 10303 (2019).
[18] A. B. Metzner and M. Whitlock, Flow Behavior of concentrated (dilatant) suspensions, Trans. Soc. Rheol. **2**, 239 (1958).
[19] J. Comtet, G. Chatté, A. Nigues, L. Bocquet, A. Siria, and A. Colin, Pairwise frictional profile between particles determines discontinuous shear thickening transition in non-colloidal suspensions, Nat. Commun. **8**, 15633 (2017).
[20] J. Singh, M. Rudman, and H. M. Blackburn, Reynolds number effects in pipe flow turbulence of generalized Newtonian fluids, Phys. Rev. Fluids **3**, 094607 (2018).
[21] S. Jie, G. Liejin, J. Jiaqiang, T. Chao, L. Yingda, F. Jiqiang, A. Ullmann, and N. Brauner, Investigation on laminar pipe flow of a non-Newtonian Carreau-extended fluid, J. Petrol. Sci. Eng. **205**, 108915 (2021).
[22] A. Arosemena and J. Solsvik, Velocity–vorticity correlations and the four-layer regime in turbulent channel flow of generalized Newtonian fluids, Eur. J. Mech. B. Fluids **91**, 1 (2022).
[23] A. A. Gavrilov and V. Y. Rudyak, Reynolds-averaged modeling of turbulent flows of power-law fluids, J. Non-Newtonian Fluid Mech. **227**, 45 (2016).
[24] Y. Matsuoka, Y. Nakayama, and T. Kajiwara, Prediction of shear thickening of particle suspensions in viscoelastic fluids by direct numerical simulation, J. Fluid Mech. **913**, A38 (2021).
[25] A. Monti and M. E. Rosti, Shear-thickening of dense bidispersed suspensions, Meccanica **58**, 727 (2023).

[26] D. T. Karahan, D. Ranjan, and C. K. Aidun, Turbulent channel flow of generalized Newtonian fluids at Re$\tau = 180$, J. Non-Newtonian Fluid Mech. **314**, 105015 (2023).
[27] P. J. Carreau, Rheological equations from molecular network theories, Trans. Soc. Rheol. **16**, 99 (1972).
[28] P. J. Carreau, D. De. Kee, and M. Daroux, An analysis of the viscous behaviour of polymeric solutions, Can. J. Chem. Eng. **57**, 135 (1979).
[29] F. Zonta, C. Marchioli, and A. Soldati, Modulation of turbulence in forced convection by temperature-dependent viscosity, J. Fluid Mech. **697**, 150 (2012).
[30] G. Soligo and M. E. Rosti, Non-Newtonian turbulent jets at low-Reynolds number, Int. J. Multiphase Flow **167**, 104546 (2023).
[31] S. Tabakova, N. Kutev, and S. Radev, Oscillatory Carreau flows in straight channels, R. Soc. Open Sci. **7**, 191305 (2020).
[32] A. Ptaszek, The role of characteristic times in rheological description of structure forming food additives, J. Food Eng. **111**, 272 (2012).
[33] F. Chenlo, R. Moreira, and C. Silva, Rheological behaviour of aqueous systems of tragacanth and guar gums with storage time, J. Food Eng. **96**, 107 (2010).
[34] W. Sittikijyothin, D. Torres, and M. P. Gonçalves, Modelling the rheological behaviour of galactomannan aqueous solutions, Carbohydrate Polymers **59**, 339 (2005).
[35] J. Kim, P. Moin, and R. Moser, Turbulence statistics in fully ceveloped channel flow at low Reynolds number, J. Fluid Mech. **177**, 133 (1987).
[36] J. Jiménez and P. Moin, The minimal flow unit in near-wall turbulence, J. Fluid Mech. **225**, 213 (1991).
[37] S. A. Orszag, Accurate solution of the Orr–Sommerfeld stability equation, J. Fluid Mech. **50**, 689 (1971).
[38] T. Tsukahara, Y. Seki, H. Kawamura, and D. Tochio, DNS of turbulent channel flow at very low Reynolds numbers, in *Fourth International Symposium on Turbulence and Shear Flow Phenomena, Williamsburg, Virginia, USA* (Begel House Inc., 2005), Vol. 3, pp. 935–940.
[39] M. A. Niederschulte, R. J. Adrian, and T. J. Hanratty, Measurements of turbulent flow in a channel at low Reynolds numbers, Exp. Fluids **9**, 222 (1990).
[40] K. Lam and S. Banerjee, On the condition of streak formation in a bounded turbulent flow, Phys. Fluids **4**, 306 (1992).
[41] S. Chernyshenko and F. Baig, The mechanism of streak formation in near-wall turbulence, J. Fluid Mech. **544**, 99 (2005).
[42] J. Jiménez, Coherent structures in wall-bounded turbulence, J. Fluid Mech. **842**, P1 (2018).
[43] J. Jiménez, Near-wall turbulence, Phys. Fluids **25**, 101302 (2013).
[44] J. M. Hamilton, J. Kim, and F. Waleffe, Regeneration mechanisms of near-wall turbulence structures, J. Fluid Mech. **287**, 317 (1995).
[45] J. Jiménez and A. Pinelli, Coherent structures in wall-bounded turbulence, J. Fluid Mech. **389**, 335 (1999).
[46] M. A. Alves, P. J. Oliveira, and F. T. Pinho, Numerical methods for viscoelastic fluid flows, Annu. Rev. Fluid Mech. **53**, 509 (2021).
[47] P. K. Ptasinski, B. J. Boersma, F. T. M. Niewuwstadt, M. A. Hulsen, B. H. A. A. Van Den Brule, and J. C. R. Hunt, Turbulent channel flow near maximum drag reduction: simulations, experiments and mechanisms, J. Fluid Mech. **490**, 251 (2003).
[48] C. Nouar, A. Bottaro, and J. P. Brancher, Delaying transition to turbulence in channel flow: Revisiting the stability of shear-thinning fluids, J. Fluid Mech. **592**, 177 (2007).
[49] E. Milocco, Repository for Laminar turbulent behavior in shear-thickening channel flow, https://doi.org/10.6084/m9.figshare.28082246.v1 (2025).